# Anisotropic cluster model for the short-range order in Cu1-xPdx-type alloys

# Anisotropic cluster model for the short-range order in $Cu_{1-x}Pd_x$-type alloys

P. De Meulenaere
*Electron Microscopy for Materials Science (EMAT), Universiteit Antwerpen (RUCA), Groenenborgerlaan 171, B-2020 Antwerpen, Belgium*

M. Rodewald
*TH Darmstadt, Fachbereich Materialwissenschaft, Fachgebiet Strukturforschung, Petersenstrasse 23, D-64287 Darmstadt, Germany*

G. Van Tendeloo
*Electron Microscopy for Materials Science (EMAT), Universiteit Antwerpen (RUCA), Groenenborgerlaan 171, B-2020 Antwerpen, Belgium*

(Received 4 August 1997)

The split diffuse maxima around the {110} and {100} positions in the diffraction pattern of short-range-ordered $Cu_{1-x}Pd_x$ alloys ($x=0.10...0.60$) are attributed to small atomic clusters, being part of the underlying fcc lattice. By analyzing the reciprocal space geometry, our cluster method identifies two prominent cluster types: the tetrahedron of nearest neighbors and a linear three-points cluster along the ⟨110⟩ directions. Since both cluster types contain different information on the same nearest-neighbor correlations, local anisotropy has to be assumed. It is shown that the three interatomic pair interactions within these basic clusters are sufficient to generate the spot splitting in the diffraction pattern. A ground-state analysis with these interactions reproduces the results of the anisotropic next-nearest-neighbor Ising model. [S0163-1829(98)02418-7]

## I. INTRODUCTION

Diffuse intensity in the diffraction patterns of many alloys is due to substitutional short-range order (SRO).[1–5] In most cases, the diffuse intensity is located at the highly symmetrical special points of the first Brillouin zone, for example, for the fcc-based alloys: $Ni_4Mo$ at $(1\frac{1}{2}0)$,[6–8] $Pd_3V$ at (100),[9,10] and CuPt at $(\frac{1}{2}\frac{1}{2}\frac{1}{2})$.[11,12]

$Cu_{1-x}Pd_x$ is interesting since it shows fourfold splitting of the SRO intensity at the {110} positions and twofold splitting at the {100} positions for $x>0.10$ (Refs. 13–16) (Fig. 1). Below the order-disorder transition temperature $T_c$, a long-period antiphase boundary (LPAPB) structure is observed for these compounds, giving satellite reflections at the same positions as in the SRO.[17,18] Following the Fermi-surface imaging theory,[19] below $T_c$, the splitting can be explained by the flattening of the Fermi surface if its double radius approaches too close to the boundaries of the first Brillouin zone. The Fermi-surface imaging theory holds as well for the SRO state:[14,20] Ohshima and Watanabe[14] describe how the splitting of the diffuse maxima in the Cu-Pd system increases with decreasing e/a (electrons per atom) ratio, i.e., with increasing Pd concentration. Other (100)-type systems exhibiting split diffuse maxima are Au-Pd,[21,22] Ag-Mg,[21] Au-Zn,[21,23] Cu-Al,[24] Cu-Zn,[25] and Cu-Au (Ref. 2) (at the onset to long-range order).

It should be noted that both diffraction and Fermi surfaces deal with *average* structures and thus are considered with respect to the full symmetry of the underlying fcc lattice. It is one of the aims of this paper to deduce very local information that does not necessarily reflect this symmetry. The present results are hence not necessarily in contradiction with the theory of Fermi-surface imaging.

In order to build a real-space configuration for the SRO in the Cu-Pd system, different routes can be followed. In Ref. 26, a configuration model was proposed, based on a distribution of $L1_2$-type microdomains, being in antiphase to each other. The average distance in between the domains was calculated from the concentration wave model.[4,27] In Ref. 28, microdomains are indeed observed in $Cu_3Pd$ by means of high-resolution electron microscopy. Rahman[29] also concluded from videographic and random-phase simulations on $Cu_3Au$, that an antiphase distribution of domains leads to the diffuse spot splitting.

Recently,[16] we studied the SRO in $Cu_{1-x}Pd_x$ by high-resolution electron microscopy. It was found that two-

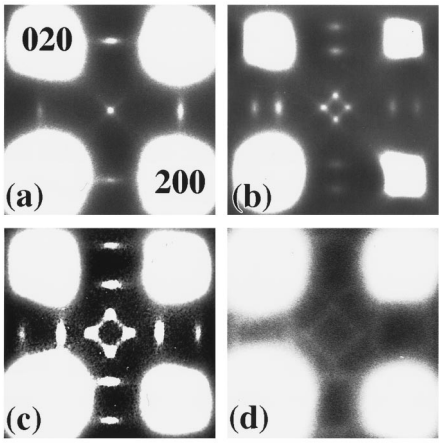


FIG. 1. [001] electron-diffraction patterns of $Cu_{1-x}Pd_x$, where $x=0.10$ (a), 0.30 (b), 0.40 (c), and 0.50 (d). In (c), the contrast is overenhanced in order to visualize the diffuse streaks, perpendicular to the twofold splitting or connecting the spots in the fourfold splitting.

 

dimensional (2D)-correlation vectors of the type $\langle n,1\rangle$ in the projected {001} planes are responsible for the splitting. This can be brought in agreement with the microdomain model when this $\langle n,1\rangle$ vector is the connection between two domains. Moreover, it was argued that these correlation vectors between just single atoms, and not necessarily domains, may also contribute to the split diffuse intensity.

Starting from the SRO parameters, calculated from x-ray diffraction, Saha and co-workers[15] compared configurations for the SRO in Cu-Pd alloys with different compositions. While the diffuse maxima were clearly split in the experimental observations, it could not directly be pointed out which structure effects in the simulated configuration were responsible for the splitting.

In the present work, we describe the splitting analytically by means of the cluster model, developed in Refs. 7 and 30–33. The principles of this method and its application to electron diffraction on the Cu-Pd system are explained in the next section. The as-found cluster model is then tested by random-phase and videographic simulations (Sec. III). In Sec. IV, a ground-state analysis is derived from the occurring clusters. The result is in agreement with the anisotropic next-nearest-neighbor Ising (ANNNI) model for second-nearest-neighbor interactions. A direct link is then made between the spot splitting and the ANNNI model for the SRO state, without the need for long-range interactions.

## II. RECIPROCAL SPACE CLUSTER ANALYSIS OF THE DIFFUSE INTENSITY

### A. Outline of the theory

The present analysis of the diffuse intensity will derive the most apparent clusters that are responsible for the SRO. The construction of such a cluster model is based on a mapping function $f(\mathbf{g})$, which is constructed in such a way that the integral

$$\int_{V^*} I_D(\mathbf{g})|f(\mathbf{g})|^2 d\mathbf{g} \tag{1}$$

is as small as possible. $I_D(\mathbf{g})$ represents the diffuse diffraction intensity and $V^*$ the volume of the reciprocal space unit cell. For the minimization of Eq. (1), $f(\mathbf{g})$ is constructed such that it vanishes on a contour in reciprocal space, which covers the maxima of $I_D(g)$. In practice, it turns out that the summation in the Fourier decomposition of $f(\mathbf{g})$,

$$f(\mathbf{g})=\sum_k \omega_k e^{-2\pi i \mathbf{g}\cdot\mathbf{r}_k}, \tag{2}$$

contains a very limited number of terms.

From Eqs. (1) and (2), one can prove[33] that in direct space

$$\varepsilon_j=\sum_{i=1}^{M} \omega_i \sigma_{j+i} \quad \forall \mathbf{r}_j, \tag{3}$$

where $\varepsilon_j$ is only a small value if Eq. (1) is small, and it is called the residue value for site $j$. The physical meaning of minimizing the integral (1) is assigned by this equation: it provides local occupations for $M$ sites, i.e., it describes frequently occurring $M$-points clusters, when Eq. (1) is small. In Eq. (3), the index $j+i$ refers to the site $\mathbf{r}_j+\mathbf{r}_i$ of the underlying lattice. $\sigma_k$ is the occupation parameter for the site $\mathbf{r}_k$, defined as follows:[34]

$$\sigma_k=\begin{cases} -m_B & \text{if the site } \mathbf{r}_k \text{ is occupied by an } A \text{ atom,} \\ m_A & \text{if the site } \mathbf{r}_k \text{ is occupied by a } B \text{ atom,} \end{cases} \tag{4}$$

and $m_A$ (resp. $m_B$) is the fraction of $A$ $(B)$ atoms, i.e.: $m_A+m_B=1$. The average of the residue values over the total number of lattice sites $N$ is always zero. Its variance can be proven to be

$$\langle|\varepsilon|^2\rangle=\frac{1}{N}\sum |\varepsilon_j|^2=\frac{1}{NV^*}\int_{V^*} I_D(\mathbf{g})|f(\mathbf{g})|^2 d\mathbf{g}. \tag{5}$$

This integral is exactly expression (1).[32] The variance can only vanish if the mapping function $f(\mathbf{g})$ is zero on all positions where the diffuse intensity is nonzero.

Equation (3) gives information about an $M$-points cluster. In many cases, this cluster can be occupied by some different configurations of $A$ and $B$ atoms, in such a way that in Eq. (3) the value $\varepsilon_j$ vanishes. The global configuration of the alloy then is a conglomerate of these clusters and probably some others for which $\varepsilon_j$ is nonzero, so that by the use of Eq. (5), the variance of the residues is obtained. For an experimental analysis including the residues, one needs quantitative diffraction data. However, when starting from an electron-diffraction experiment, one usually approximates the problem by restricting the diffuse intensity to a confined locus, so that the residue effectively becomes zero. The resulting clusters then describe approximately the real configuration. This purely geometrical approach however does not take dynamical diffraction into account.

### B. Tetrahedron of nearest neighbors

Figure 1 shows the [001] electron-diffraction patterns for different concentrations of the Cu-Pd alloy. The split diffuse maxima are for all concentrations located on the lines $h$, $k$, or $l=$ odd. These lines coincide exactly with the contours $f(\mathbf{g})=0$, where we propose for the mapping function:

$$f(\mathbf{g})\equiv f(h,k,l)=1+\exp[i\pi(h+k)]+\exp[i\pi(h-l)] + \exp[i\pi(k-l)]. \tag{6}$$

From this, the corresponding cluster relation is

$$\sigma_i+\sigma_{i+(1/2,1/2,0)}+\sigma_{i+(1/2,0,1/2)}+\sigma_{i+(0,1/2,1/2)}=0 \quad \forall \mathbf{r}_i. \tag{7}$$

This relation defines the four lattice sites of a tetrahedron of nearest neighbors [Fig. 2(a)]. The cluster relation (7) can be fulfilled for an $A_3B$ and for an $AB$ composition. When stacking, e.g., the $A_3B$ clusters, and keeping in mind that Eq. (7) must hold for all lattice sites, one can build the $L1_2$ superstructure, the $DO_{22}$ superstructure and many intermediate variants in between these [Fig. 2(b)]. $B$-$B$ atom pairs never occur on nearest-neighbor sites. In Ref. 33, it is indeed proved that the cluster relation (7) is a consequence of repulsive nearest-neighbor interatomic interactions. In Ref. 35, this tetrahedron cluster has been applied to the $Pt_3V$ system to describe the transition from the 100 type of SRO to the $DO_{22}$ superstructure. In the case of the $AB$ composition, Eq.

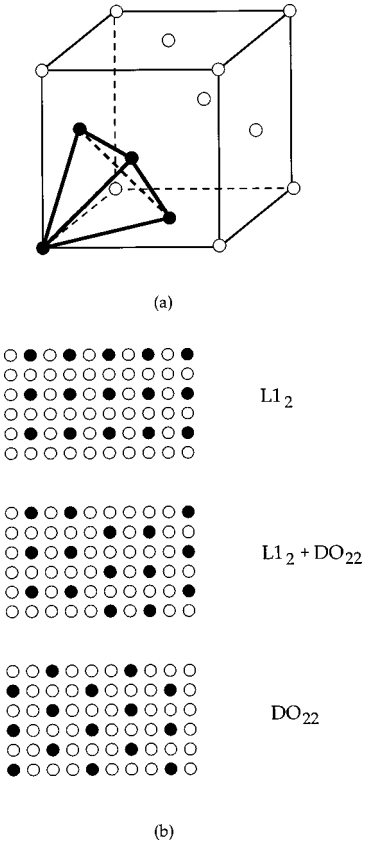


FIG. 2. (a) Tetrahedron (in bold) of nearest neighbors in an fcc cube. (b) Examples of stacking an $A_3B$ structure so that Eq. (7) is fulfilled for all lattice sites. Only two nonoverlapping (001) layers have been drawn. Empty circles represent $A$ atoms, filled circles, $B$ atoms.

(7) also includes the $L1_0$ structure and the so-called $A_2B_2$ structure,[36] which belongs to the $1\frac{1}{2}0$ type of alloys. For other compositions, one has to admit nonzero residues in Eq. (7).

### C. Linear three-points cluster

Simultaneous with the splitting, one observes weak diffuse lines in the diffraction patterns, passing through the diffuse maxima [Fig. 1(c)]. In order to relate a cluster type to the origin of these diffuse lines, we propose 6 mapping functions, given by the equations

$$f(\mathbf{g}) = \omega + \exp[i\pi(h \pm l)] + \exp[-i\pi(h \pm l)],$$

$$f(\mathbf{g}) = \omega + \exp[i\pi(k \pm l)] + \exp[-i\pi(k \pm l)],$$

$$f(\mathbf{g}) = \omega + \exp[i\pi(h \pm k)] + \exp[-i\pi(h \pm k)]. \qquad (8)$$

The zero contours of these mapping functions are planes in reciprocal space. Their section with the plane $l=0$ is represented in Fig. 3. The parameter $\omega$ in Eq. (8) influences the distance of splitting and depends only on the composition. As can be seen in Fig. 3, these planes cover much more of the reciprocal space than the observed diffuse intensities, but expression (1) is still minimized. The associated cluster relation will therefore be too general to give a complete description of the real configuration, but one has to keep in

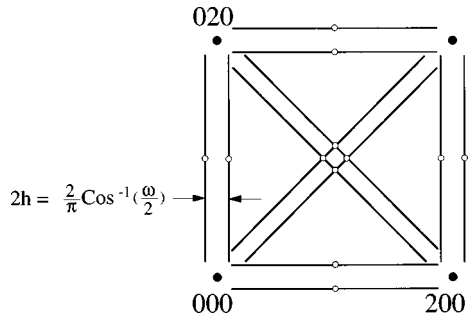


FIG. 3. Contours for which the mapping functions $f(\mathbf{g})$ from Eq. (8) are zero in the [001] section.

mind that the tetrahedron of nearest neighbors [Eq. (7)] simultaneously imposes its own conditions on the configuration. Ohshima and Watanabe[14] observe a slight curvature of the diffuse lines, which is in correspondence with the Fermi-surface imaging theory. However, these curvatures manifest themselves only at the very ends of the diffuse streaks and hence give very weak deviations from the present assumptions. For most compounds, they are even invisible. This small deviation thus will result in a residue value, which will be very small.

From Eq. (8), we find six equivalent clusters, being linear three-points clusters along the ⟨110⟩ directions (Fig. 4), described by the relation

$$\sigma_{i+a} + \omega\sigma_{i+b} + \sigma_{i+c} = \varepsilon_i \quad \forall \mathbf{r}_i . \qquad (9)$$

For arbitrary values of $\omega$, i.e., for most splitting distances, the residue $\varepsilon_i$ in Eq. (9) can never vanish. Note that the original problem is now reduced to six equivalent one-dimensional problems. Thus we have to construct a linear chain of atoms that minimizes the variance $\langle|\varepsilon|^2\rangle$ for Eq. (9).

For some special values of $\omega$, the residue value in Eq. (9) may vanish. These values and the corresponding chains are enumerated in Table I. They vary from homogeneous chains ($\omega=-2$, no splitting), to an alternation of $A$ and $B$ atoms ($\omega=2$, extreme splitting up to the (110) reflections). These chains can now be coupled to their neighboring chains by applying Eq. (7) of the tetrahedron of nearest neighbors. Figure 5 shows the results for some of the cases from Table I. For a global $AB$ composition of the alloy, $\omega=-2$ and $\omega=2$ result in two different variants of the $L1_0$ structure [Figs. 5(a) and 5(c)] and $\omega=0$ gives the $A_2B_2$ structure [Fig. 5(b)]. For the $A_3B$ composition, the $L1_2$ structure can be generated by stacking pure $A$ and $AB$ rows. The diffraction pattern of the $L1_2$ structure can indeed be covered by simultaneously two mapping functions: one for $\omega=-2$ and one for $\omega$

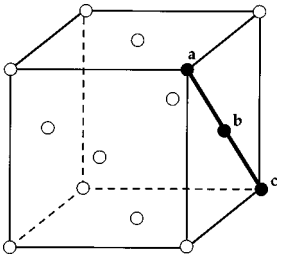


FIG. 4. The linear three-points cluster (in bold), consisting of the sites $a$, $b$, and $c$, along one of the ⟨110⟩ directions.

TABLE I. All possible clusters with vanishing residues for the linear three-points cluster.

| $\omega$ | Possibilities for cluster fillings | Chain examples | Global composition |
|---|---|---|---|
| $-2$ | $AAA$ | $\ldots AAAAAAA\ldots$ | $A$ |
| $-2$ | $BBB$ | $\ldots BBBBBBBBB\ldots$ | $B$ |
| 0 | $AAB$ or $ABB$ or $BAA$ or $BBA$ | $\ldots AABBAABB\ldots$ | $AB$ |
| 1 | $AAB$ or $ABA$ or $BAA$ | $\ldots AABAABAAB\ldots$ | $A_2B$ |
| 1 | $BBA$ or $BAB$ or $ABB$ | $\ldots BBABBABBA\ldots$ | $AB_2$ |
| 2 | $ABA$ or $BAB$ | $\ldots ABABABAB\ldots$ | $AB$ |

$=2$. In the case of SRO, the reflections are diffuse and the residue values are consequently nonzero. Therefore, the periodic chains from Table I will only have a limited length.

Nonzero residue values have also to be allowed for arbitrary splitting distances and for alloy compositions for which the cluster relation (9) cannot be fulfilled. A detailed treatment of Eq. (9) will provide us with the cluster fillings that minimize the variance $\langle|\varepsilon|^2\rangle$. Indeed, by the use of definition (4), Eq. (9) can also be written as

$$\varepsilon_i = -m_B(2+\omega)+X+\omega Y, \tag{10}$$

where $X$ is the number of $B$ atoms on sites $a$ and $c$ (thus $X=0$, 1, or 2) and $Y$ is the number of $B$ atoms on site $b$ (thus $Y=0$ or 1) of the cluster with index $i$. In Ref. 33, one proves that a lower bound for the variance $\langle|\varepsilon|^2\rangle$ is given by $-\varepsilon_i\varepsilon_{i+1}$, where $\varepsilon_i$ is the largest negative and $\varepsilon_{i+1}$ is the smallest positive residue value, determined by variation of $X$ and $Y$ in Eq. (10). The two cluster types found then have to be used in the chain formation in order to minimize $\langle|\varepsilon|^2\rangle$. Table II summarizes these pairs of minimizing clusters and some examples of chains; $\omega$ and $m_B$ are found from the experiment (e.g., from Fig. 1). In some of the chains, other clusters than the minimizing clusters have to be introduced, in order to realize the stacking or to fulfill the global composition. In such cases, the obtained variance $\langle|\varepsilon|^2\rangle$ will be larger than the predicted lower bound $-\varepsilon_i\varepsilon_{i+1}$.

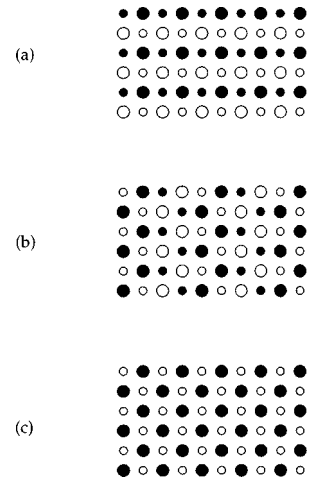


FIG. 5. Some structures, resulting from stacking the linear three-points clusters, for which the variance is zero. (a) and (c) two variants of $L1_0$ ($\omega=-2$ and $\omega=2$); (b) $A_2B_2$ ($\omega=0$). Empty circles represent $A$ atoms, filled circles, $B$ atoms; small and large circles represent atoms on different heights.

Close to the value $\omega=-2$, the configuration will tend to separate $A$- and $B$-type atoms (within a chain). These long homogeneous chains appear in $L1_0$ or $L1_2$ microdomains. From $\omega=-1$ on, pairs of $B$ atoms will occur separately in the majority of $A$ atoms (for $m_A>m_B$). When $\omega=0$, the zero contours of the mapping functions cross the $\{1\frac{1}{2}0\}$ positions. From Eq. (10), it appears that in this particular case, the value of $Y$ does not influence the residue value, while $X$ has to be 0 or 1. It is then possible to build, e.g., $\ldots AAABAAAB\ldots$ chains, which, when combined with the tetrahedron relation (7), can give rise to a $DO_{22}$ microdomain. This is globally the expected evolution in $Cu_{1-x}Pd_x$, where $\omega$ remains negative (as can be measured from Fig. 1). By varying $\omega$, a continuous series of structures is thus found, which describe the transition from the (100)- to the $(1\frac{1}{2}0)$-type of SRO.

## III. DIRECT-SPACE SIMULATIONS

### A. Random-phase simulations

The present cluster model cannot predict the size of the ordered chains or the distance in between the microdomains, but the concentration wave model[4,27] can. In the one-dimensional problem, diffuse spot splitting with a spot at position $h$ [see inset in Fig. 6(a) for the definition of the distance $h$], results in a concentration wave, described by a continuous occupation parameter

$$\sigma(x) = -\tfrac{1}{2}\cos(2\pi i h x+\varphi), \tag{11}$$

where $\varphi$ is an arbitrary phase factor. Equation (11) gives a zero residue value in Eq. (9) for $\omega=-2\cos(\pi h)$. The full three-dimensional problem can be treated by superimposing all occurring concentration waves (11) for the different directions. Random-phase simulations then put random-phase factors $\varphi$ in the different concentration waves. In Fig. 6(a), a 2D-domain configuration is shown for a splitting distance $h=\frac{1}{16}$, obtained by the random-phase method. 2D-correlation vectors of the type $\langle n,1\rangle$ and $\langle n,n+1\rangle$ are found in-between the domains, where $n=1/h$ and $n$ can be related to the chain length of the chains described in Table II. The presence of $APB$'s [Fig. 6(b)] is due to the tetrahedron relation (7). For instance, for an $AB$ composition, when a chain of $B$ atoms breaks down, a chain of $A$ atoms has to follow. The neighboring row to this one consequently must have the opposite occupation. In this way, a configuration of domains is built by stacking chains of length $n$, combined with the presence of $APB$'s. This generates correlation vectors of the

TABLE II. Clusters that minimize $\langle|\varepsilon|^2\rangle$ as a function of $\omega$, for the case $m_A \geqslant m_B$. If $m_A \leqslant m_B$, the symbols $A$ and $B$ have to be interchanged.

| $\omega$ | | $(X,Y)$ in Eq. (10) | | Clusters | | Chain examples | |
|---|---|---|---|---|---|---|---|
| $m_B \leqslant \frac{1}{3}$ | $m_B \geqslant \frac{1}{3}$ | $m_B \leqslant \frac{1}{3}$ | $m_B \geqslant \frac{1}{3}$ | $m_B \leqslant \frac{1}{3}$ | $m_B \geqslant \frac{1}{3}$ | $m_B \leqslant \frac{1}{3}$ | $m_B \geqslant \frac{1}{3}$ |
| $-2 \leqslant \omega \leqslant -1$ | | (0,0) | | $AAA$ | | …$AAAAABBBBB$… | |
| | | (2,1) | | $BBB$ | | | |
| $-1 \leqslant \omega \leqslant \frac{m_B}{m_A} - 1$ | | (1,0) | | $BAA$ or $AAB$ | | …$AABBAABBAABB$… | |
| | | (1,1) | | $BBA$ or $ABB$ | | | |
| $\frac{m_B}{m_A} - 1 \leqslant \omega \leqslant 0$ | | (0,0) | | $AAA$ | | …$AABBAABBAABB$… or more $A$: | |
| | | (1,1) | | $BBA$ or $ABB$ | | …$AAAAABBAAABBAAAAA$… | |
| $0 \leqslant \omega \leqslant 2\frac{m_B}{m_A}$ | | (1,0) | (1,0) | $BAA$ or $AAB$ | $BAA$ or $AAB$ | …$BAABAABAA$… | …$AABBAABB$… |
| | $0 \leqslant \omega \leqslant 1$ | (0,1) | (1,1) | $ABA$ | $BBA$ or $ABB$ | | |
| $2\frac{m_B}{m_A} \leqslant \omega \leqslant 1$ | | (0,0) | | $AAA$ | | …$ABAAAABAA$… | |
| | | (0,1) | | $ABA$ | | | |
| $1 \leqslant \omega \leqslant \frac{1}{m_B} - 2$ | | (0,0) | (2,0) | $AAA$ | $BAB$ | …$ABAAAABAA$… | …$ABABABAB$… |
| | $1 \leqslant \omega \leqslant 2$ | (1,0) | (0,1) | $BAA$ or $AAB$ | $ABA$ | | |
| $\frac{1}{m_B} - 2 \leqslant \omega \leqslant 2$ | | (1,0) | | $BAA$ or $AAB$ | | …$ABABABAB$… | |
| | | (2,0) | | $BAB$ | | | |

type $\langle n, n+1, 1\rangle$ in between the domains, which give in projection the 2D correlations in Fig. 6(a).

### B. Videographic simulations

The amplitude of the concentration wave is connected to the intensity of the corresponding diffraction spot and influences therefore the actual size of the ordered microdomains. Since for SRO the intensity is very low, the domain size is expected to be very small, maybe only one or a few unit cells. The size can even be further reduced so that one obtains just a distribution of single atoms connected by the correct correlation vector. From a detailed high-resolution electron microscopy study,[16] evidence is found that this can indeed be the case in Cu-Pd alloys. To test this model, different types of unit cells are distributed on an fcc lattice, connected by vectors of the type $\langle n, n+1, 1\rangle$. These simulations are performed by the videographic simulation method.[29,37]

For all of these simulations, a diffraction pattern is found that exhibits the split diffuse spots with the correct spot splitting. Figure 7 shows the extreme case where just single $B$ atoms are distributed in a large simulation box. The correlation vectors are of the type $\langle 4, 5, 1\rangle$, as indicated in the enlarged part of the simulation field [Fig. 7(a)]. The diffraction pattern [Fig. 7(b)] shows the geometry of the spot splitting, similar to Fig. 1. Simulations were also performed for small chains of $B$ atoms, $L1_2$ microdomains, and $L1_0$ microdomains. They all lead to similar patterns as in Fig. 7(b).

## IV. GROUND-STATE ANALYSIS

### A. Outline of the method

Van Dyck *et al.*[32] prove that for an arbitrary mapping function $f(\mathbf{g})$, one always has

$$\langle|\varepsilon|^2\rangle = \frac{1}{NV^*}\int_{V^*} I_D(\mathbf{g})|f(\mathbf{g})|^2 d\mathbf{g} = m_A m_B \sum_{i,k} \omega_i \alpha_{i-k} \omega_k \geqslant 0, \tag{12}$$

where $f(\mathbf{g})$ follows Eq. (2). $\alpha_{i-k}$ is the SRO parameter (Refs. 1–5) for the interatomic distance $\mathbf{r}_i - \mathbf{r}_k$. The summation in Eq. (12) can be written in matrix notation as

$$\langle|\varepsilon|^2\rangle = m_A m_B \langle\omega|\alpha|\omega\rangle \geqslant 0, \tag{13}$$

with $|\omega\rangle$ a vector with elements $\omega_i$, and $\alpha$ a matrix with elements $\alpha_{i,j} = \alpha_{(i-j)}$. From the basic knowledge that $I_D(\mathbf{g})$ is positive, one finds in Eq. (13) that the $\alpha$ matrix has to be positive definite, which gives restrictions on the possible values of $\alpha$. This can be visualized in the $\alpha$ space where an existency domain or configuration polyhedron can be constructed wherein Eq. (13) holds. The boundaries of this domain correspond to $\langle|\varepsilon|^2\rangle = 0$, whereas within the polyhe-

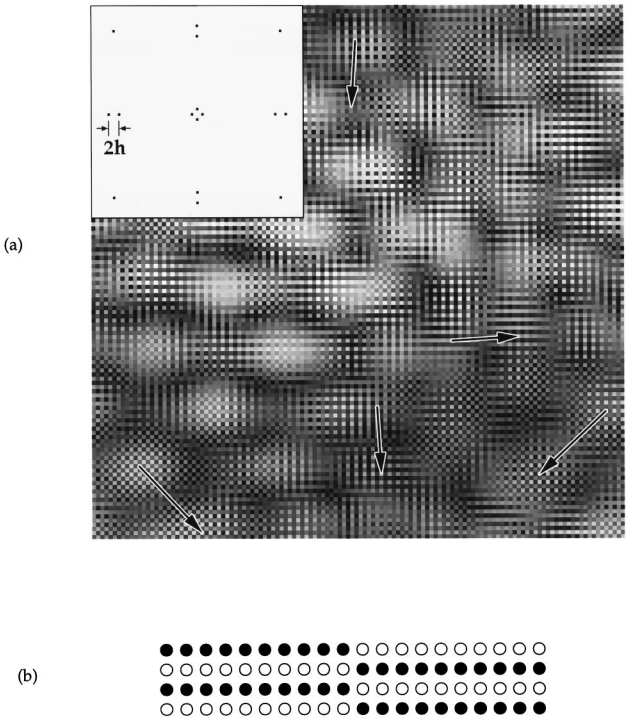


FIG. 6. (a) 2D random-phase simulation for $h=\frac{1}{16}$. Full white pixels represent $A$ atoms, full black represents $B$. The indicated arrows are of the type $\langle n,1\rangle$ or $\langle n,n+1\rangle$, and are hence perpendicular to the APB's in between the small domains. The inset shows the diffraction pattern. (b) APB formation in the $L1_0$ structure. Resulting from the stacking rule of the tetrahedron, Eq. (7), an APB is formed at the spot where the horizontal homogeneous chains break down.

dron $\langle|\varepsilon|^2\rangle>0$. Outside the domain, it is impossible to stack any structure with the given $\alpha$'s. This method has been applied in order to construct the existency domain in many types of basic structures.[33,38] An alternative method for the ground-state analysis is constructing the Kanamori inequalities for the clusters.[39] The derivation of the interatomic interactions is then done in dual space, which is similar to what we will do in Sec. V.

### B. Tetrahedron of nearest neighbors

In Ref. 33, one derives the existency domain for the tetrahedron of nearest neighbors. Since only nearest neighbors are present within this small cluster, the $\alpha$ space is one dimensional, and the boundaries of the polyhedron are defined by

$$-\tfrac{1}{3}\leqslant\alpha_1\leqslant 1. \tag{14}$$

At the boundary $\alpha_1=-\frac{1}{3}$, the corresponding eigenvector is defined by the elements $\omega_1=\omega_2=\omega_3=\omega_4=1$. This eigenvector defines exactly the mapping function of Eq. (6).

### C. Linear three-points cluster

Within the linear three-points cluster, the nearest and the fourth-nearest neighbor on the fcc lattice are present, their SRO parameters being denoted here by $\beta_1$, resp. $\beta_2$. The matrix of SRO parameters then is

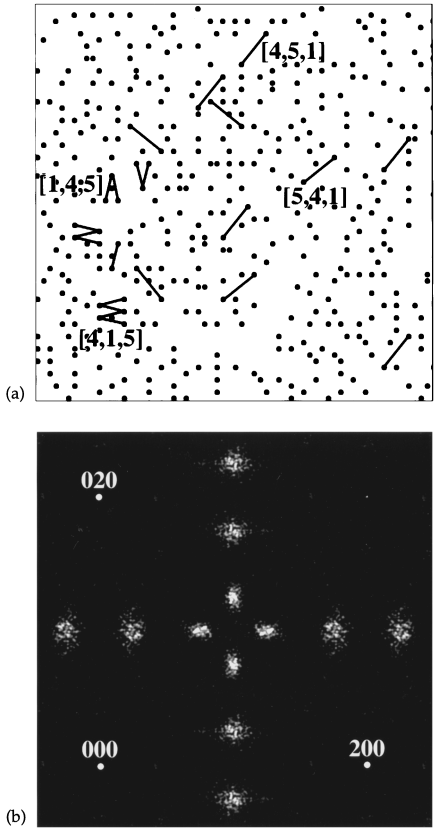


FIG. 7. (a) Part of the simulation field of a 3D videographic simulation. Points are distributed with preference for the correlation vectors $\langle 4,5,1\rangle$. Some of these vectors are indicated. (b) Corresponding diffraction pattern for the full simulation. The spot splitting is clearly present.

$$\begin{pmatrix} 1 & \beta_1 & \beta_2 \\ \beta_1 & 1 & \beta_1 \\ \beta_2 & \beta_1 & 1 \end{pmatrix}. \tag{15}$$

The existency domain is bound by the curves $1-\beta_2=0$ and $1-2\beta_1^2+\beta_2=0$ and is shown in Fig. 8 in $(\beta_1,\beta_2)$ space. For $\beta_2=1$, the corresponding eigenvector is $(1,0,-1)$. For the boundary $1-2\beta_1^2+\beta_2=0$, the corresponding eigenvector is $(1,\omega,1)$, $\omega=-2\beta_1$. This eigenvector results in the mapping functions (8). Note that the relationship $\omega=-2\beta_1$ only holds exactly on the boundaries, i.e., when $\langle|\varepsilon|^2\rangle=0$. For SRO, it is thus not possible to derive $\beta_1$ from the splitting distance.

For a configuration exactly at the boundary of the existency domain, the diffracted intensity has to appear strictly on the zero contours of the mapping function. At the corners of the existency domain, superstructure reflections will hence occur for a structure having the corresponding SRO parameters. For Fig. 8, the resulting superstructures are mentioned. They are exactly the ones that also result from the ANNNI model with second-nearest-neighbor interactions.[5,40]

## V. DISCUSSION: CORRESPONDENCE TO THE ANNNI MODEL

The parameters $\alpha_1$ in the nearest-neighbor tetrahedron and $\beta_1$ in the linear three-points cluster both give informa-

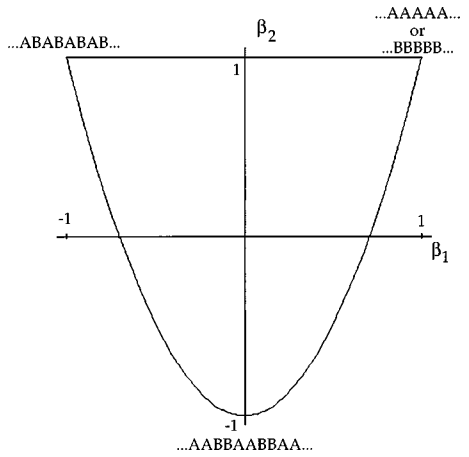


FIG. 8. Existency domain for the linear-chain problem with two neighbors. Within the figure, it is possible to build one-dimensional configurations with the corresponding SRO parameters $(\beta_1,\beta_2)$. Out of the figure, it is mathematically impossible to stack the corresponding structure. At the edges, the corresponding superstructures are mentioned.

tion on the same type of correlation. In the present model they are uncoupled however, so that we have to assume local anisotropy to apply the model. Within the framework of Ising models for alloys, the ANNNI model provides the possibility to introduce anisotropy. In order to prove that our anisotropic cluster model is equivalent to the ANNNI model, we have to ''translate'' our results in function of the interatomic pair interactions.

In a binary fcc alloy, the internal energy $U$ per fcc unit cell is given by[2]

$$U = m_A m_B \sum_{i=1}^{p} Z_i \alpha_i V_i , \tag{16}$$

where $Z_i$ is the number of lattice sites in the $i$th neighboring shell, $\alpha_i$ the corresponding SRO parameter, and $V_i$ the corresponding pair interaction parameter. Equation (16) represents a hyperplane in the $p$-dimensional $\alpha$ space. Upon ordering, the internal energy decreases and the plane (16) moves parallel to itself to one of the corners in the existency domain, until a superstructure is realized. This relationship between existency domain, superstructures, and interaction parameters results in a phase diagram that subdivides the interaction space in different regions, indicating which phase is expected to be the ground state.[4,5,33,41]

For the easy case of nearest-neighbor interactions within the tetrahedron, the phase diagram discerns only $V_1<0$, corresponding to segregation in pure $A$ and pure $B$ phases, and $V_1>0$, which can, e.g., result in $L1_0$, $L1_2$, or $DO_{22}$.

From the positions of the three superstructures in the existency domain of the linear three-points cluster, the phase diagram in $(J_1,J_2)$ space is derived (Fig. 9). The interaction parameters are now denoted by $J$ in order not to be confused with $V_1$.[42] The phase diagram discerns the phase segregation $\langle\infty\rangle$ (…$AAA$… coexisting with …$BBB$…, equivalent to ferromagnetism), the phase $\langle 1\rangle$ (…$ABABAB$…, or antiferromagnetism) and the phase $\langle 2\rangle$ (…$AABBAABB$…). Exactly the same ground-state phase diagram has been calculated for

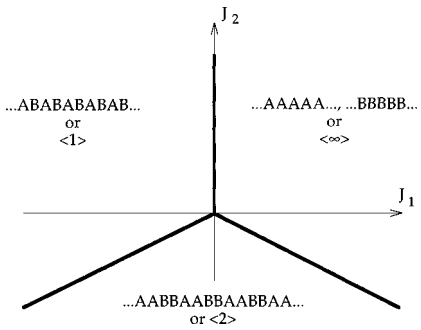


FIG. 9. Phase diagram for the one-dimensional Ising problem with second-nearest-neighbor interactions. The ANNNI model exhibits the same diagram.

the ANNNI model with second-nearest-neighbor interactions.[5,40] Within the concept of the Ising model, one has the possibility to examine the configuration for nonzero temperatures and it has been shown that the occurrence of LPAPB structures, which are stable below $T_c$ for a broad composition range in Cu-Pd alloys, can be explained by this ANNNI model.[40] This justifies that anisotropic interactions also can be introduced for the SRO.

In order to prove that this limited set of interactions $V_1$, $J_1$, and $J_2$ can account for the split diffuse intensity in the SRO state, we calculate the minima of the potential $V(\mathbf{g})$ in reciprocal space. Consider therefore a chain along the [011] direction, starting from the central black atom in Fig. 10(a). Two sites for each of the interactions $J_1$ and $J_2$ and 12 nearest neighbors for interaction $V_1$ are available, so that

$$\begin{aligned} V(\mathbf{g}) = & -2J_1\cos[\pi(k+l)] - 2J_2\cos[2\pi(k+l)] \\ & + 2V_1\{\cos[\pi(h+k)] + \cos[\pi(h-k)] \\ & + \cos[\pi(h+l)] + \cos[\pi(h-l)] \\ & + \cos[\pi(k+l)] + \cos[\pi(k-l)]\}. \end{aligned} \tag{17}$$

This function is represented in Fig. 10(b) [and the profile for $h=1$ in Fig. 10(c)] in the [001] section. Its minima reproduce part of the split intensities in the diffraction pattern. The other split spots are obviously obtained when the other chain directions are included. The mathematical analogy between Eq. (17) and the construction of the different mapping functions (6) and (8) is also apparent.

When the internal energy $U$ in Eq. (16) decreases, the line of constant energy $U$ can shift in Fig. 8 until it coincides with the tangent of the parabola. The tangent line can be described as

$$\beta_2 = -2\omega\beta_1 + C, \tag{18}$$

where $C$ is a constant. On the other hand, Eq. (16) shows a similar linear dependence between the SRO parameters $\beta_1$ and $\beta_2$, from which follows

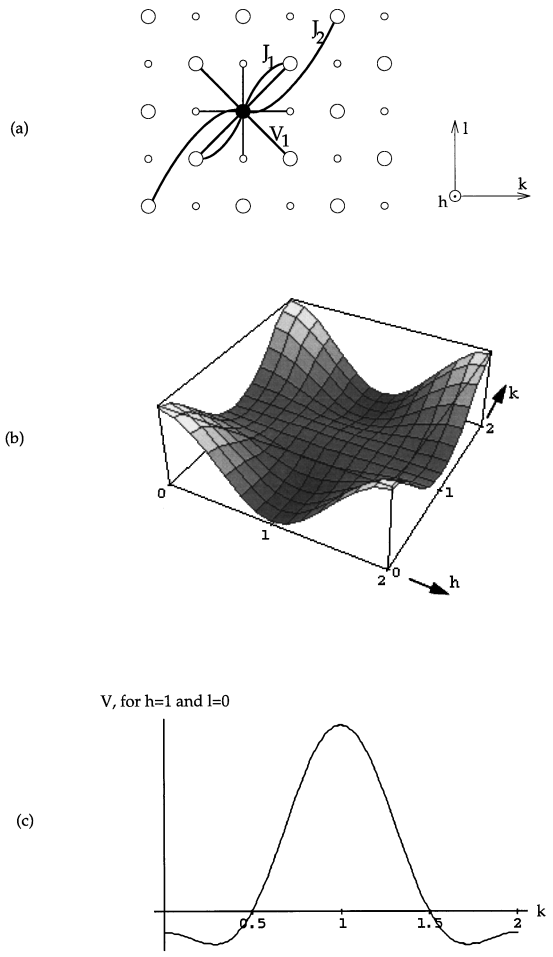


FIG. 10. (a) $V_1$, $J_1$, and $J_2$ in a specific example. Small and large dots represent atoms on different heights. (b) Plot of $V(\mathbf{g})$ in the [001] section ($V_1=+0.30$, $J_1=+0.25$, $J_2=-0.10$, arbitrary units). (c) Profile of (b) for $h=1$.

$$\frac{J_1}{J_2}=2\omega, \tag{19}$$

which also results from a straightforward calculation of the minima of Eq. (17). This relationship between the parameter $\omega$ and the interaction parameters $J$ can be used to confirm another standard result of the ANNNI model: close to $T_c$, concentration waves in the SRO (or paramagnetic) state are found to occur with a characteristic wavelength

$$q_c=\cos^{-1}\left(\frac{J_1}{4|J_2|}\right) \quad \text{with } \frac{J_1}{|J_2|}\leqslant 4. \tag{20}$$

With the use of Eq. (19), Eq. (20) exactly reproduces the zero contours of the mapping functions (8).

The strength of the above conclusion lies in the fact that, if anisotropy is introduced, only very few parameters are needed for the generation of diffuse split diffraction maxima. The split intensities can be reproduced in isotropic models as well, but it is then to be expected that many interatomic interactions have to be taken into account, even 30 or more as one can conclude from, e.g., Ref. 15. In Ref. 43 one however shows that a simple isotropic Hamiltonian can reproduce many of the features of the phase diagram of the ANNNI model. With just a small set of interplanar interactions (essentially four), they simulate many characteristics of the LPAPB's in the Cu-Pd system. It should be noticed that these interplanar interactions are to be interpreted as a parametrization of many interatomic interactions—the authors mention that one should make calculations up to at least the 40th neighbor effective pair interaction. The success of the use of interplanar interactions is to be found in the fact that the dimensionality of the problem is reduced, which is in essence the introduction of an anisotropic effect. A correspondence with the ANNNI model has indeed been drawn in Ref. 43, and it has been concluded that the interplanar interactions are equivalent to the interactions of the ANNNI model. This sustains the observations of the present paper.

## VI. CONCLUSIONS

It is well known that multiple scattering gives an important contribution to electron diffraction. Electron-diffraction patterns can therefore not be used to derive detailed quantitative results. The mapping function in the present cluster method uses in first instance only the loci of the diffuse intensity, not the numerical value of this intensity. It is therefore a very suitable, but only qualitative, method for the interpretation of SRO in electron diffraction.

The cluster analysis first gives the almost trivial tetrahedron of nearest neighbors which, as much as possible, has to be filled out with the macroscopic composition. From the ground-state analysis, this means that the interatomic potential for nearest-neighbor lattice sites is repulsive for chemically equivalent atoms.

The splitting of the diffuse intensity maxima is introduced in the model by the linear three-points cluster via the parameter $\omega$. Variation of the value of $\omega$ allows a continuous transition between different one-dimensional chain occupations, which results in a transition from the (100)- to the $(1\frac{1}{2}0)$-type of SRO. The occupation of the chain can alternatively be governed by a concentration wave model. This concentration wave is, for most values of $\omega$, incommensurate with respect to the fcc structure and hence gives site occupations that are not purely $A$ or $B$. The cluster analysis is therefore closer to a realistic description, but has to allow a nonzero variance $\langle|\varepsilon|^2\rangle$.

Combining the tetrahedron cluster and the linear three-points cluster, the importance of the correlation vectors $\langle n,n+1,1\rangle$ is derived and illustrated by direct-space simulations.

The ground-state analysis for the linear three-points cluster proves that the ANNNI model with second-nearest-neighbor interactions provides the basic features of the system, also in its SRO state. An immediate and causal connection is hence drawn between a specific type of SRO diffuse intensity contours and the possibility of an anisotropic interaction model for the Hamiltonian of the alloy.

## ACKNOWLEDGMENTS

M.R. acknowledges IUAP 48 and IUAP 4/10 for financial support during his stay at EMAT-RUCA.

[1] J. M. Cowley, Phys. Rev. **77**, 669 (1950).
[2] P. C. Clapp and S. C. Moss, Phys. Rev. **142**, 418 (1966); **171**, 754 (1968); S. C. Moss and P. C. Clapp, *ibid.* **171**, 764 (1968).
[3] M. A. Krivoglaz, *Theory of X-Ray and Thermal-Neutron Scattering by Real Crystals* (Plenum, New York, 1969).
[4] D. de Fontaine, Solid State Phys. **34**, 73 (1979).
[5] F. Ducastelle, *Order and Phase Stability in Alloys* (North-Holland, Amsterdam, 1991).
[6] J. E. Spruiell and E. E. Stansbury, J. Phys. Chem. Solids **26**, 811 (1965); B. Chackravarti, E. A. Starke, Jr., C. J. Sparks, and R. O. Williams, *ibid.* **35**, 1317 (1974).
[7] R. De Ridder, G. Van Tendeloo, and S. Amelinckx, Acta Crystallogr., Sect. A: Cryst. Phys., Diffr., Theor. Gen. Crystallogr. **32**, 216 (1976).
[8] G. Van Tendeloo, S. Amelinckx, and D. de Fontaine, Acta Crystallogr., Sect. B: Struct. Sci. **41**, 281 (1985).
[9] D. Schryvers and S. Amelinckx, Acta Metall. **34**, 43 (1986).
[10] F. Solal, R. Caudron, F. Ducastelle, A. Finel, and A. Loiseau, Phys. Rev. Lett. **58**, 2245 (1987).
[11] J.-P. Chevalier and W. M. Stobbs, Acta Metall. **27**, 285 (1979).
[12] E. Torfs, L. Stals, J. Van Landuyt, P. Delavignette, and S. Amelinckx, Phys. Status Solidi A **22**, 45 (1974).
[13] D. Watanabe, J. Phys. Soc. Jpn. **14**, 436 (1959).
[14] K. Ohshima and D. Watanabe, Acta Crystallogr., Sect. A: Cryst. Phys., Diffr., Theor. Gen. Crystallogr. **29**, 520 (1973).
[15] D. K. Saha, K. Koga, and K. Ohshima, J. Phys.: Condens. Matter **4**, 10 093 (1992).
[16] M. Rodewald, K. Rodewald, P. De Meulenaere, and G. Van Tendeloo, Phys. Rev. B **55**, 14 173 (1997).
[17] D. Watanabe and S. Ogawa, J. Phys. Soc. Jpn. **11**, 226 (1956); **12**, 259 (1957).
[18] D. Broddin, G. Van Tendeloo, J. Van Landuyt, S. Amelinckx, R. Portier, M. Guymont, and A. Loiseau, Philos. Mag. A **54**, 395 (1986); D. Broddin, G. Van Tendeloo, J. Van Landuyt, S. Amelinckx, and A. Loiseau, Philos. Mag. B **57**, 31 (1988).
[19] H. Sato and R. S. Toth, Phys. Rev. Lett. **8**, 239 (1962).
[20] S. C. Moss, Phys. Rev. Lett. **22**, 1108 (1969); B. L. Gyorffy and G. M. Stocks, *ibid.* **50**, 374 (1983).
[21] K. Ohshima and D. Watanabe, Acta Crystallogr., Sect. A: Cryst. Phys., Diffr., Theor. Gen. Crystallogr. **33**, 784 (1977).
[22] W. Lin, J. E. Spruiell, and R. O. Williams, J. Appl. Crystallogr. **3**, 297 (1970).
[23] G. Van Tendeloo and S. Amelinckx, Phys. Status Solidi A **50**, 53 (1978).
[24] B. Borie and C. J. Sparks, Jr., Acta Crystallogr. **17**, 827 (1964); R. O. Scattergood, S. C. Moss, and M. B. Bever, Acta Metall. **18**, 1087 (1970).
[25] L. Reinhard, B. Schönfeld, G. Kostorz, and W. Bürher, Z. Metallkd. **84**, 251 (1993).
[26] S. Hashimoto, Acta Crystallogr., Sect. A: Cryst. Phys., Diffr., Theor. Gen. Crystallogr. **30**, 792 (1974).
[27] A. G. Khachaturyan, Phys. Status Solidi B **60**, 9 (1973).
[28] G. Van Tendeloo and S. Amelinckx, Phys. Status Solidi A **77**, K9 (1983).
[29] S. H. Rahman, Acta Crystallogr., Sect. A: Found. Crystallogr. **49**, 68 (1993).
[30] R. De Ridder, G. Van Tendeloo, D. Van Dyck, and S. Amelinckx, Phys. Status Solidi A **38**, 663 (1976).
[31] R. De Ridder, D. Van Dyck, G. Van Tendeloo, and S. Amelinckx, Phys. Status Solidi A **40**, 669 (1977).
[32] D. Van Dyck, R. De Ridder, G. Van Tendeloo, and S. Amelinckx, Phys. Status Solidi A **43**, 541 (1977).
[33] D. Van Dyck, R. De Ridder, and S. Amelinckx, Phys. Status Solidi A **59**, 513 (1980).
[34] P. A. Flinn, Phys. Rev. **104**, 350 (1956).
[35] D. Schryvers, G. Van Tendeloo, and S. Amelinckx, Mater. Res. Bull. **20**, 361 (1985); D. Schryvers and S. Amelinckx, Res. Mech. **22**, 101 (1987).
[36] U. D. Kulkarni, S. Muralidhar, and S. Banerjee, Phys. Status Solidi A **110**, 331 (1988).
[37] S. H. Rahman, Acta Crystallogr., Sect. A: Found. Crystallogr. **49**, 56 (1993); S. H. Rahman and M. Rodewald, *ibid.* **51**, 153 (1995).
[38] R. De Ridder, D. Van Dyck, and S. Amelinckx, Phys. Status Solidi A **61**, 231 (1980); L. Van Goethem, Ph.D. thesis, Universiteit Antwerpen, 1982; D. Schryvers and D. Van Dyck, Philos. Mag. A **56**, 115 (1987).
[39] J. Kanamori, Prog. Theor. Phys. **35**, 16 (1966); M. Kaburagi and J. Kanamori, *ibid.* **54**, 30 (1975).
[40] J. Yeomans, Solid State Phys. **41**, 151 (1988).
[41] A. Finel, in *L'Ordre et le Désordre dans les Matériaux* (Les Éditions de Physique, Les Ulis, France, 1984).
[42] For the derivation of the phase diagram in $(J_1, J_2)$ space, the internal energy in Eq. (16) has first been multiplied by $-1$. Consequently, when $V_1 > 0$ means ordering, $J_1 > 0$ means phase separation. We have applied this illogical notation in order to be consistent with the literature, where the Hamiltonian of the ANNNI model indeed includes opposite signs for $V_1$ and $J_1$.
[43] G. Ceder, D. de Fontaine, H. Dreysse, D. M. Nicholson, G. M. Stocks, and B. L. Gyorffy, Acta Metall. Mater. **38**, 2299 (1990).